A Fast Cartesian Grid-Based Integral Equation Method for Unbounded Interface Problems with Non-Homogeneous Source Terms

Jiahe Yang[1] and Wenjun Ying[2,*]

[1] *School of Mathematical Sciences,*
Shanghai Jiao Tong University, Minhang, Shanghai 200240, P.R. China.
[2] *Department of Mathematics, MOE-LSC and Institute of Natural Sciences,*
Shanghai Jiao Tong University, Minhang, Shanghai 200240, P.R. China.

Abstract. This work presents a fast Cartesian grid-based integral equation method for unbounded interface problems with non-homogeneous source terms. The unbounded interface problem is solved with boundary integral equation methods such that infinite boundary conditions are satisfied naturally. This work overcomes two difficulties. The first difficulty is the evaluation of singular integrals. Boundary and volume integrals are transformed into equivalent but much simpler bounded interface problems on rectangular domains, which are solved with FFT-based finite difference solvers. The second one is the expensive computational cost for volume integrals. Despite the use of efficient interface problem solvers, the evaluation for volume integrals is still expensive due to the evaluation of boundary conditions for the simple interface problem. The problem is alleviated by introducing an auxiliary circle as a bridge to indirectly evaluate boundary conditions. Since solving boundary integral equations on a circular boundary is so accurate, one only needs to select a fixed number of points for the discretization of the circle to reduce the computational cost. Numerical examples are presented to demonstrate the efficiency and the second-order accuracy of the proposed numerical method.

AMS subject classifications: 35J05, 65N06, 65N38

Key words: Interface problem, unbounded domain, boundary integral equation, kernel-free method, auxiliary circle, Cartesian grid method, fast algorithm.

1   Introduction

Elliptic partial differential equations (PDEs) on unbounded domains arise in many physics and engineering problems, including solid and fluid mechanics [29, 33], electromagnetic

and mechanical wave propagation [12, 17], molecular dynamics [25] and geophysics [9]. In numerical computations, the unboundedness of the domain complicates the effective numerical solution of the problems.

Over the past decades, a large number of numerical methods for PDEs on unbounded domains have been developed. One frequently used approach is to truncate the unbounded domain and impose appropriate boundary conditions, including Dirichlet-to-Neumann (DtN) artificial boundary conditions [26–28], radiation boundary conditions [2, 16], absorbing boundary conditions [1], perfectly matched layers [4, 5], and perfect absorbing layers [40]. One of the other well-established methods is the spectral method. Among the many spectral approaches, one class employs a transform that maps a bounded domain to an unbounded domain and then uses mapped orthogonal functions [7, 15, 32]. Some others choose orthogonal basis in unbounded domains, including Hermite and Laguerre functions [30, 37, 38]. We recommend a review article [31].

Boundary integral methods (BIMs) have been used extensively in elliptic PDEs because of their ability to handle complex geometry and unbounded domains [21]. BIMs use boundary integrals to represent solutions. For PDEs on unbounded domains, the far-field condition is incorporated into the representation itself, and they are transformed into integral equations on the boundary. It reduces space dimensions of the problem by one and achieves optimal computational complexity when combined with fast algorithms. For non-homogeneous PDEs, there is a volume integral term. It brings large computational complexity which weakens the advantage of dimension reduction. Two major difficulties of solving BIMs are singular and nearly singular integrals evaluation and the high time complexity for numerical calculation.

Some methods can overcome the difficulty of singular and nearly singular integrals. One class of methods are based on quadrature schemes, including [3, 8, 19]. They achieve high accuracy by making corrections or adding quadrature points. Another class of methods evaluates singular integrals by solving PDEs [6, 42]. The integral boundary is embedded into a rectangle, and the integral can be represented by the solution to an equation on the rectangular domain.

The kernel-free boundary integral method [41–44] belongs to the second class. The singular or nearly singular boundary or volume integral evaluation requires solving an equivalent but much simpler interface problem on a rectangle. The rectangular domain is discretized with a uniform Cartesian grid and the operator is approximated by the finite difference scheme. Since Boundary and volume integrals or their derivatives are discontinuous, the finite difference scheme loses accuracy when its stencils across the integral curve. These inaccurate parts are modified by corrections, which are calculated with density functions of boundary and volume integrals. To keep the finite difference matrix unchanged, these corrections are added to the right-hand side. For equations on Cartesian grids, fast and high-accuracy solvers are readily available, such as FFT-based solvers and geometry multigrid methods.

This work proposes a fast and accurate method to evaluate boundary and volume integrals for elliptic PDEs on two-dimensional unbounded domains. Enlighten by the

kernel-free boundary integral method, boundary and volume integrals are transformed into equivalent but much simpler bounded interface problems on rectangular domains, where fast PDE solvers are readily applicable. For PDEs on bounded domains, some homogeneous boundary conditions are typically imposed on the rectangular domain boundary. However, for unbounded problems, boundary conditions on the rectangular domain are represented by boundary or volume integrals themselves to match the far-field conditions, where explicit Green's functions are required. The boundary conditions for single and double layer integrals are evaluated by the composite trapezoidal quadrature. However, the quadrature for volume integral involves extra computational costs. For this reason, the information on the rectangular boundary is compressed into that on an auxiliary circle. The compression process requires evaluating volume integrals on discretization points of the circle. The decompression process consists of solving a boundary integral equation (BIE) on the circle and evaluating double layer integrals on the rectangular boundary. It is enough to use fixed low Degrees of Freedom (DoFs) on the circle since the high convergence rate of solving BIEs with circular boundaries. In an $n \times n$ Cartesian grid, the complexity for evaluating volume integrals on the rectangular boundary directly is $\mathcal{O}(n^3)$. This compression-decompression strategy reduces it to $\mathcal{O}(Mn^2)$, where M is the DoFs of the auxiliary circle and $M \ll n$.

The proposed method (1) interprets far-field conditions as boundary and volume integrals on rectangular boundaries, which are exact, (2) solves PDEs on Cartesian grids, where fast solvers are readily applicable, (3) does not need to evaluate nearly singular boundary integral and singular volume integral, (4) evaluates volume integrals on rectangular boundaries indirectly with the compression-decompression technique, which reduces the computational complexity from $\mathcal{O}(n^3)$ to $\mathcal{O}(Mn^2)$, where n is the DoFs on each side of the rectangle and M is the fixed low DoFs on the auxiliary circle, (5) achieves optimal order of accuracy.

The remainder of this paper is organized as follows. Section 2 describes the unbounded integral problem. Subsequent sections address the BIEs for the unbounded integral problem (Section 3.1); the equivalent but much simpler bounded interface problems of boundary and volume integrals (Section 3.2); details of computing boundary conditions of simple interface problems (Section 4.1); discretization of the simple interface problem on the rectangular domain (Section 4.2). Section 5 gives a summary of the algorithm. Numerical examples are displayed in Section 6, followed by a brief discussion of future work in Section 7.

2   Unbounded interface problems

Consider an unbounded second-order elliptic interface problem defined on the two-dimensional space $\mathbb{R}^2$. Assume the interface consists of K smooth curves, denotes as $\Gamma = \cup_{k=1}^{K} \Gamma^{(k)}$. The PDEs on two sides of the interface are different. Let $\Omega_i = \cup_{k=1}^{K} \Omega^{(k)}$ be a multi-connected bounded open set with the boundary Γ, and the remaining unbounded

domain is denoted by Ω_e or $\Omega^{(0)}$. See Fig. 1(a) for illustration. Lowercase boldfaced letters **p** and **q** are used to denote points in $\mathbb{R}^2$. The outward unit normal vector at a point **p** on Γ is denoted by $\mathbf{n_p}$, pointing from the bounded domain Ω_i to the unbounded domain Ω_e. Let $u_\mathbf{n}$ or $\partial_\mathbf{n} u$ be the normal derivative of a function u on Γ and σ_i and σ_e be two positive constant conductivities of two sides respectively.

Let f_i be a smooth function defined on Ω_i, g and j are functions defined on Γ. Suppose $u_i(\mathbf{p})$ and $u_e(\mathbf{p})$ are two unknown functions in $\mathbb{R}^2$. Let κ_i and κ_e be positive real numbers. The interface problem is given by

$$\sigma_i \Delta u_i(\mathbf{p}) - \kappa_i u_i(\mathbf{p}) = f_i(\mathbf{p}), \quad \mathbf{p} \text{ in } \Omega_i, \tag{2.1}$$

$$\sigma_e \Delta u_e(\mathbf{p}) - \kappa_e u_e(\mathbf{p}) = 0, \quad \mathbf{p} \text{ in } \Omega_e, \tag{2.2}$$

subject to two interface conditions

$$u_i - u_e = g, \quad \sigma_i \partial_\mathbf{n} u_i - \sigma_e \partial_\mathbf{n} u_e = j, \quad \text{on } \Gamma, \tag{2.3}$$

and a far-field condition

$$u_e(\mathbf{p}) \text{ satisfies a suitable assumption at infinity.} \tag{2.4}$$

The condition at infinity for an elliptic equation in two dimensions may read as follows [18]:

- (Poisson equation)

$$u(\mathbf{p}) = \frac{1}{2\pi} \Sigma \log|\mathbf{p}| + \omega + o(1), \quad \text{as } |\mathbf{p}| \to \infty,$$

- (modified Helmholtz equation)

$$u \to 0, \quad \text{as } |\mathbf{p}| \to \infty.$$

For the sake of clarity, the constant conductivities σ_i and σ_e are divided into (2.1) and (2.2), respectively. The resulting elliptic operators are $\mathcal{A}_i := \Delta - \kappa_i'$, $\mathcal{A}_e = \Delta - \kappa_e'$, and the source term of (2.1) is f_i', where $\kappa_i' = \kappa_i / \sigma_i$, $\kappa_e' = \kappa_e / \sigma_e$, and $f_i' = f_i / \sigma_i$. Without loss of generality, κ_i', κ_e', f_i' are still denoted by κ_i, κ_e, f_i.

3 Boundary integral equations

3.1 The boundary integral formulation for the unbounded problem

The free-space Green functions associated with the elliptic operators $\mathcal{A}_i$ and $\mathcal{A}_e$ are denoted by $G_i(\mathbf{q}, \mathbf{p})$ and $G_e(\mathbf{q}, \mathbf{p})$, respectively, which satisfy

$$\mathcal{A}_i G_i(\mathbf{q}, \mathbf{p}) = \delta(\mathbf{q}, \mathbf{p}), \quad \mathcal{A}_e G_e(\mathbf{q}, \mathbf{p}) = \delta(\mathbf{q}, \mathbf{p}).$$
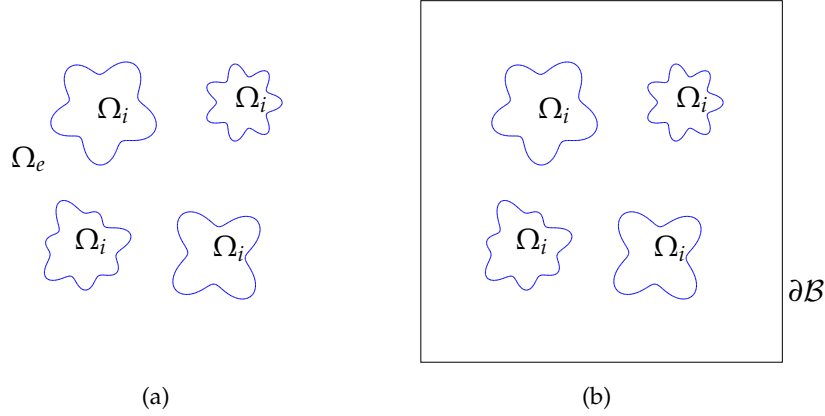
Figure 1: The unbounded interface problem is defined in $\mathbb{R}^2$, as (a) illustrated. The equivalent but much simpler bounded interface problem for evaluating the boundary or volume integral is defined on the rectangular domain, as (b) illustrated.

Here $\delta(\mathbf{q}-\mathbf{p})$ is the Dirac delta function. For the Laplace operator Δ and the modified Helmholtz operator $\Delta-\kappa^2$, the Green functions in two dimensions are

$$\frac{1}{2\pi}\ln|\mathbf{q}-\mathbf{p}|, \quad -\frac{1}{2\pi}K_0(\kappa|\mathbf{q}-\mathbf{p}|).$$

Here K_0 is the zeroth-order modified Bessel function of the second kind [13]. In the following paragraphs, if there is no confusion, the subscripts $_i$ or $_e$ are omitted.

Define the volume integral on Ω by

$$(\mathcal{G}f)(\mathbf{p}):=\int_\Omega G(\mathbf{q},\mathbf{p})f(\mathbf{p})\,\mathrm{d}\mathbf{q}.$$

Let $H^{1/2}(\Gamma)$ be the trace space of Sobolev space $H^1(\Omega)$ on $\Gamma=\partial\Omega$ and $H^{-1/2}(\Gamma)$ be the dual space of $H^{1/2}(\Gamma)$. Let $\mathbf{n_p}$ be the unit outward vector at point $\mathbf{p}\in\Gamma$. For density function $\varphi\in H^{1/2}(\Gamma)$, define the double layer boundary integral by

$$(\mathcal{M}\varphi)(\mathbf{p}):=\int_\Gamma \frac{\partial G(\mathbf{p},\mathbf{q})}{\partial\mathbf{n_q}}\varphi(\mathbf{q})\,\mathrm{d}s_\mathbf{q}\in H^{1/2}(\Gamma)$$

and the hyper-singular boundary integral by

$$(\mathcal{N}\varphi)(\mathbf{p}):=\int_\Gamma \frac{\partial^2 G(\mathbf{p},\mathbf{q})}{\partial\mathbf{n_q}\partial\mathbf{n_p}}\varphi(\mathbf{q})\,\mathrm{d}s_\mathbf{q}\in H^{-1/2}(\Gamma).$$

For density function $\psi\in H^{-1/2}(\Gamma)$, define the single layer boundary integral by

$$(\mathcal{L}\psi)(\mathbf{p}):=\int_\Gamma G(\mathbf{p},\mathbf{q})\psi(\mathbf{q})\,\mathrm{d}s_\mathbf{q}\in H^{1/2}(\Gamma)$$

and the adjoint double layer boundary integral by

$$(\mathcal{M}^*\psi)(\mathbf{p}) := \int_\Gamma \frac{\partial G(\mathbf{p,q})}{\partial \mathbf{n_p}} \psi(\mathbf{q}) \, ds_\mathbf{q} \in H^{-1/2}(\Gamma).$$

The symbol with a subscript, e.g. $\mathcal{M}_i$ or $\mathcal{M}_e$, indicates the corresponding Green's functions are G_i or G_e. Functions on the two-dimensional space are denoted by lowercase letters when density functions are clear, i.e., $w := \mathcal{M}\varphi$, $s := -\mathcal{L}\psi$, $w_\mathbf{n} := \mathcal{N}\varphi$, $s_\mathbf{n} := -\mathcal{M}^*\psi$, $v = \mathcal{G}f$.

Note that

$$K_0(x) \sim -\ln(x) + P(x), \quad \text{as } x \to 0,$$

where $P(x)$ is a polynomial. Therefore, the Green function of modified Helmholtz behaves asymptotically as if it has a logarithmic kernel [23]. The jump relations for potentials of the logarithmic kernel are well-known [18]. One-sided limits are represented by notations u^+ and u^-, i.e.,

$$u^+ := \lim_{\substack{\mathbf{p} \in \Omega_i \\ \mathbf{p} \to \Gamma}} u(\mathbf{p}), \quad u^- := \lim_{\substack{\mathbf{p} \in \Omega_e \\ \mathbf{p} \to \Gamma}} u(\mathbf{p}).$$

The double layer integral w has a jump discontinuity on Γ but the normal derivative $w_\mathbf{n}$ is continuous

$$\begin{aligned} w^+(\mathbf{p}) &= \frac{1}{2}\varphi(\mathbf{p}) + (\mathcal{M}\varphi)(\mathbf{p}), \\ w^-(\mathbf{p}) &= -\frac{1}{2}\varphi(\mathbf{p}) + (\mathcal{M}\varphi)(\mathbf{p}). \end{aligned} \tag{3.1}$$

The single layer integral s is continuous on Γ while its normal derivative $s_\mathbf{n}$ has a jump discontinuity

$$\begin{aligned} s_\mathbf{n}^+(\mathbf{p}) &= \frac{1}{2}\psi(\mathbf{p}) - (\mathcal{M}^*\psi)(\mathbf{p}), \\ s_\mathbf{n}^-(\mathbf{p}) &= -\frac{1}{2}\psi(\mathbf{p}) - (\mathcal{M}^*\psi)(\mathbf{p}). \end{aligned} \tag{3.2}$$

Introducing two unknown functions on Γ,

$$\varphi(\mathbf{p}) = u_i(\mathbf{p}), \quad \psi(\mathbf{p}) = \sigma_e \partial_\mathbf{n} u_e(\mathbf{p}), \tag{3.3}$$

by Green's second identity, and definitions of g, j, ϕ and ψ, the solution $u(\mathbf{p})$ of the interface problem (2.1)-(2.4) is expressed in terms of boundary and volume integrals of the form

$$u_i = \mathcal{M}_i\varphi - \frac{1}{\sigma_i}(\mathcal{L}_i\psi + \mathcal{L}_i j) + \mathcal{G}_i f_i \quad \text{in } \Omega_i, \tag{3.4}$$

$$u_e = -\mathcal{M}_e\varphi + \frac{1}{\sigma_e}\mathcal{L}_e\psi + \mathcal{M}_e g \quad \text{in } \Omega_e. \tag{3.5}$$

Letting **p** in Eq. (3.4) approach to the boundary Γ from inside, and in (3.5) approach to the boundary from outside, one obtains two boundary integral equations

$$\frac{1}{2}\varphi = \mathcal{M}_i\varphi - \frac{1}{\sigma_i}\mathcal{L}_i\psi - \frac{1}{\sigma_i}\mathcal{L}_i j + \mathcal{G}_i f_i \quad \text{on } \Gamma, \tag{3.6}$$

$$\frac{1}{2}(\varphi - g) = -\mathcal{M}_e\varphi + \frac{1}{\sigma_e}\mathcal{L}_e\psi + \mathcal{M}_e g \quad \text{on } \Gamma. \tag{3.7}$$

Computing normal derivatives of (3.4) or (3.5), one is led to another two equations

$$\frac{1}{2}(\psi + j) = \sigma_i\mathcal{N}_i\varphi - \mathcal{M}_i^*\psi - \mathcal{M}_i^* j + \sigma_i\partial_\mathbf{n}\mathcal{G}_i f_i \quad \text{on } \Gamma, \tag{3.8}$$

$$\frac{1}{2}\psi = -\sigma_e\mathcal{N}_e\varphi + \mathcal{M}_e^*\psi + \sigma_e\mathcal{N}_e g \quad \text{on } \Gamma. \tag{3.9}$$

Adding Eqs. (3.6) and (3.7) together, and Eqs. (3.8) and (3.9) together, one reformulates the interface problem (2.1)-(2.4) on an unbounded domain as a system of two boundary integral equations

$$\varphi - \mathcal{M}_i\varphi + \mathcal{M}_e\varphi + \frac{1}{\sigma_i}\mathcal{L}_i\psi - \frac{1}{\sigma_e}\mathcal{L}_e\psi = \frac{1}{2}g + \mathcal{G}_i f_i - \frac{1}{\sigma_i}\mathcal{L}_i j + \mathcal{M}_e g, \tag{3.10}$$

and

$$\psi - \sigma_i\mathcal{N}_i\varphi + \sigma_e\mathcal{N}_e\varphi + \mathcal{M}_i^*\psi - \mathcal{M}_e^*\psi = -\frac{1}{2}j + \sigma_i\partial_\mathbf{n}\mathcal{G}_i f_i - \mathcal{M}_i^* j + \sigma_e\mathcal{N}_e g. \tag{3.11}$$

Remark that in the special case when $\mathcal{A}_i = \mathcal{A}_e$, the solution can be expressed as an indirect formulation

$$u(\mathbf{p}) = \mathcal{M}g(\mathbf{p}) - \mathcal{L}\zeta(\mathbf{p}) + \mathcal{G}f_i(\mathbf{p}), \quad \text{in } \mathbb{R}^2, \tag{3.12}$$

where the unknown density function $\zeta(\mathbf{p}) = \partial_\mathbf{n}u_i - \partial_\mathbf{n}u_e, \mathbf{p} \in \Gamma$. Computing the normal derivative of (3.12) in Ω_i and Ω_e, respectively, and applying jump relations (3.2), one is led to the following equations

$$\partial_\mathbf{n}u^+ = \mathcal{N}g + \left(\frac{1}{2}\mathbf{I} - \mathcal{M}^*\right)\zeta + \partial_\mathbf{n}\mathcal{G}f \quad \text{on } \Gamma, \tag{3.13}$$

$$\partial_\mathbf{n}u^- = \mathcal{N}g - \left(\frac{1}{2}\mathbf{I} + \mathcal{M}^*\right)\zeta + \partial_\mathbf{n}\mathcal{G}f \quad \text{on } \Gamma. \tag{3.14}$$

Here **I** is the identity operator. Combining Eqs. (3.13)-(3.14) together with jump conditions (2.3) yields the boundary integral equation

$$\frac{1}{2}\zeta + \mu\mathcal{M}^*\zeta = \mu(\mathcal{N}g + \partial_\mathbf{n}\mathcal{G}f) + \nu j, \quad \mathbf{p} \in \Gamma, \tag{3.15}$$

where $\mu = (\sigma_e - \sigma_i)/(\sigma_e + \sigma_i), \nu = 1/(\sigma_e + \sigma_i)$.

There are plenty of methods to discretize integral equations in literature, including quadrature methods and projection methods [20]. This work evaluates the boundary or

volume integral by solving an equivalent but much simpler bounded interface problem on a rectangular domain. The equivalent simple interface problems are explained in the next subsection.

The resulting linear systems can be solved with iterative methods [11]. For non-symmetric linear systems, the Krylov subspace method [35, 36, 45, 46] are widely used. In this work, the integral equation is solved with the generalized minimal residual (GM-RES) method.

3.2 Equivalent simple interface problems

With the continuity properties of the boundary and volume integrals listed in Eqs. (3.1) and (3.2), each of these integrals is reinterpreted as a solution to an equivalent but much simpler bounded interface problem on a rectangular domain. The rectangular domain $\mathcal{B}$ is artificially selected so that it can properly embed the interface Γ and is sufficiently far from it to avoid nearly singular integrals. See Fig. 1(b) for illustration.

For a function u, let $[u]:=u^+-u^-$ and $[u_{\mathbf{n}}]:=u_{\mathbf{n}}^+-u_{\mathbf{n}}^-$ be the jump of one-sided limits of u and its normal derivative across the interface Γ. The volume integral v satisfies the interface problem

$$
\begin{aligned}
\mathcal{A}u &= \tilde{f}, && \text{in } \mathcal{B}, \\
[u] &= 0, && \text{on } \Gamma, \\
[u_{\mathbf{n}}] &= 0, && \text{on } \Gamma, \\
u &= \mathcal{G}f, && \text{on } \partial\mathcal{B}.
\end{aligned}
\tag{3.16}
$$

Here $\tilde{f}$ is discontinuous, defined as

$$
\tilde{f}(\mathbf{p}) = \begin{cases} f(\mathbf{p}), & \mathbf{p}\in\Omega_i, \\ 0, & \mathbf{p}\notin\Omega_i. \end{cases}
$$

The double layer integral w is the unique solution to the following interface problem

$$
\begin{aligned}
\mathcal{A}u &= 0, && \text{in } \mathcal{B}, \\
[u] &= \varphi, && \text{on } \Gamma, \\
[u_{\mathbf{n}}] &= 0, && \text{on } \Gamma, \\
u &= \mathcal{M}\varphi, && \text{on } \partial\mathcal{B}.
\end{aligned}
\tag{3.17}
$$

The single layer potential s is the unique solution to the following interface problem

$$
\begin{aligned}
\mathcal{A}u &= 0, && \text{in } \mathcal{B}, \\
[u] &= 0, && \text{on } \Gamma, \\
[u_{\mathbf{n}}] &= \psi, && \text{on } \Gamma, \\
u &= -\mathcal{L}\psi, && \text{on } \partial\mathcal{B}.
\end{aligned}
\tag{3.18}
$$

In the simple interface problems (3.16), (3.17) and (3.18), the explicit Green's function is used to compute boundary conditions. Since the rectangular boundary is far enough from the interface, integrals are nonsingular, the composite trapezoidal quadrature requires only a few points to compute boundary integrals. The equivalence between each of these interface problems and the corresponding boundary or volume integral is proved in [44].

4 Evaluation of integrals

Evaluating boundary and volume integrals are transformed into solving these simple interface problems (3.16)-(3.18). Suppose the boundary conditions on the rectangular domain are obtained, then the domain is partitioned into a uniform Cartesian grid, and the PDE is discretized with a corrected finite difference scheme and solved by FFT-based fast elliptic solvers. Singular integrals on the interface Γ are evaluated by two-variable Lagrange polynomial interpolations.

4.1 Integrals on the rectangular boundary

This subsection explains how to compute boundary conditions of simple interface problems. More specifically, the evaluation of boundary and volume integrals on the rectangular boundary $\partial \mathcal{B}$ is displayed. Unlike bounded problems [39, 44], the boundary condition on the rectangular boundary is nontrivial, which is given by the explicit integral formulation. Evaluating boundary conditions of simple interface problems avoid singular and nearly singular integrals, provided the rectangular boundary is not too close to the interface. The composite trapezoidal quadrature is used to evaluate double and single layer integrals since it achieves spectral accuracy for periodic functions. However, the computational cost for evaluating volume integral directly is expensive. If the rectangular domain is partitioned into a uniform $n \times n$ Cartesian grid, then the integral domain Ω_i consists of $\mathcal{O}(n^2)$ cells generally. The operations needed for evaluating v at each point is $\mathcal{O}(n^2)$, and the total cost for the boundary condition computation is $\mathcal{O}(n^3)$. In contrast, evaluating boundary integrals at all boundary nodes needs $\mathcal{O}(n^2)$ operations.

To improve the efficiency of evaluating volume integrals, we introduce an auxiliary circle in the integral evaluation procedure, which can be understood as a compression-decompression process. Depending on the location of the auxiliary circle, there are two versions of the method.

4.1.1 The first version

The auxiliary circle is chosen so that $\Omega_i \subset \Omega_0 \subset \mathcal{B}$. We solve a homogeneous exterior Dirichlet boundary value problem with BIMs, which is highly accurate, and then the density function on Γ_0 is used to compute volume integrals on $\partial \mathcal{B}$, see Fig. 2(a) for illus-

tration. The exterior Dirichlet BVP with boundary Γ_0 reads,

$$
\begin{aligned}
\mathcal{A}_i u &= 0 \quad \text{in } \bar{\Omega}_0^c, \\
u &= \mathcal{G}f \quad \text{on } \Gamma_0.
\end{aligned}
\tag{4.1}
$$

Here $\mathcal{A}_i$ is the inside elliptic operator of the original interface problem. The unknown function u satisfies a suitable far-field condition:

$$
u(\mathbf{p}) = \frac{1}{2\pi} \Sigma \log|\mathbf{p}| + \omega + o(1) \quad \text{for the 2D Laplace operator;}
$$

$$
u(\mathbf{p}) \to 0 \quad \text{for the 2D modified Helmholtz operator.}
$$

The exterior Dirichlet boundary value problem is solved efficiently with BIMs. The indirect boundary integral equation is formulated as

$$
-\frac{1}{2}\phi(\mathbf{p}) + \int_{\Gamma_0} \frac{\partial G(\mathbf{q},\mathbf{p})}{\partial \mathbf{n}} \phi(\mathbf{q}) \, ds_{\mathbf{q}} = \mathcal{G}f(\mathbf{p}) - u_\infty(\mathbf{p}), \quad \mathbf{p} \in \Gamma_0.
\tag{4.2}
$$

Here ϕ is an unknown density function on the boundary Γ_0, and u_∞ is an asymptotic approximation of u at infinity. The solution is a double layer integral

$$
u(\mathbf{p}) = \int_{\Gamma_0} \frac{\partial G(\mathbf{q},\mathbf{p})}{\partial \mathbf{n}} \phi(\mathbf{q}) \, ds_{\mathbf{q}} + u_\infty(\mathbf{p}).
\tag{4.3}
$$

For the modified Helmholtz operator, $K_0(r) \sim \sqrt{\pi/2r}e^{-r}$, so the volume integral $v(\mathbf{p}) \sim 0$ when $|\mathbf{p}| \to \infty$. For the Laplace operator, when $|\mathbf{p}| \to \infty$,

$$
v(\mathbf{p}) := \frac{1}{2\pi} \int_\Omega \ln|\mathbf{q}-\mathbf{p}| f(\mathbf{q}) \, d\mathbf{q} \sim \frac{1}{2\pi} \ln|\mathbf{q}_0-\mathbf{p}| \int_\Omega f(\mathbf{q}) \, d\mathbf{q},
$$

the dominant term is $\mathcal{O}(\log r)$, where $\mathbf{q}_0$ is an arbitrary point in Ω.

4.1.2 The second version

The second version suppose that Γ_0 is outside the rectangle $\mathcal{B}$, i.e., $\Omega_i \subset \mathcal{B} \subset \Omega_0$. We solve a non-homogeneous interior Dirichlet BVP, and, similar to the first version, use the density function on Γ_0 to compute volume integrals on $\partial\mathcal{B}$. Since the IDP is non-homogeneous, we introduce a larger rectangle $\tilde{\mathcal{B}}$ to compute a special solution, then use BIMs to solve a homogeneous BVP, see Fig. 2(b) for illustration.

The non-homogeneous interior Dirichlet BVP is

$$
\begin{aligned}
\mathcal{A}v &= \tilde{f} \quad \text{in } \Omega_0, \\
v &= \mathcal{G}f \quad \text{on } \Gamma_0,
\end{aligned}
\tag{4.4}
$$

and the special solution v_1 satisfies

$$
\begin{aligned}
\mathcal{A}v_1 &= \tilde{f} \quad \text{in } \tilde{\mathcal{B}}, \\
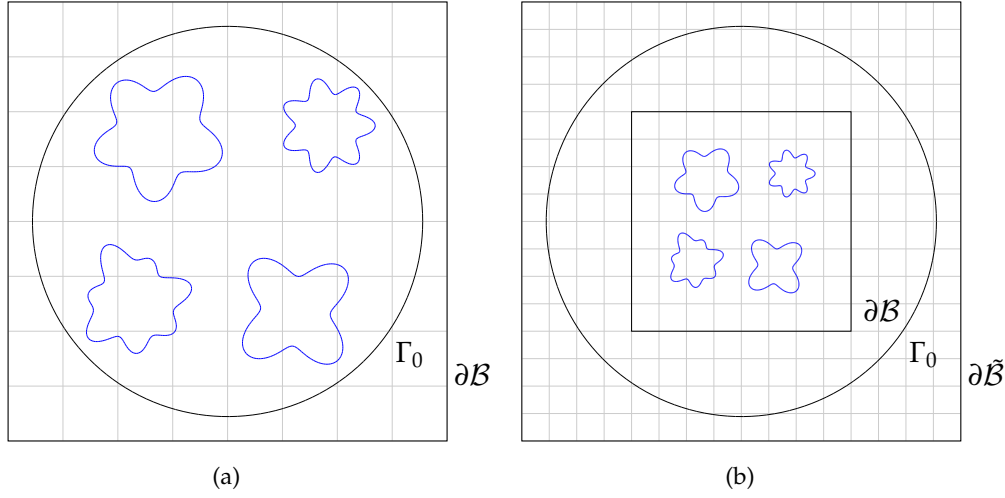v_1 &= 0 \quad \text{on } \partial\tilde{\mathcal{B}},
\end{aligned}
\tag{4.5}
$$

Figure 2: The compression-decompression technique is implemented with an auxiliary circle Γ_0. The compression process is computing volume integrals at fixed low DoFs of discretization points of Γ_0. (a) Γ_0 is located between the interface Γ and the rectangular boundary $\partial \mathcal{B}$. The decompression solves an exterior Dirichlet BVP and evaluates double layer potentials on the rectangular boundary. (b) Γ_0 is outside the rectangular domain, and a bigger rectangle $\tilde{\mathcal{B}}$ is introduced. The decompression solves an interior Dirichlet BVP.

and v_2 (solution to a homogeneous BVP) satisfies

$$
\begin{aligned}
\mathcal{A}v_2 &= 0 \quad \text{in } \Omega_0, \\
v_2 &= \mathcal{G}f - v_1 \quad \text{on } \Gamma_0,
\end{aligned}
\tag{4.6}
$$

where $\tilde{\mathcal{B}}$ is the bigger rectangle, and $\Omega_i \subset \mathcal{B} \subset \Omega_0 \subset \tilde{\mathcal{B}}$. Then $v_1 + v_2$ is the unique solution to (4.4). Eq. (4.5) is discretized with a corrected finite difference scheme and solved with FFT-based solvers, and (4.6) is solved with BIMs.

The first technique is straightforward. But it needs the prior information for the asymptotic expansion of the volume integral to match the far-field conditions [18]. The second technique requires a bigger rectangle and a special solution. Both of them can reduce the computational complexity of evaluating volume integrals on the rectangular boundary to $\mathcal{O}(Mn^2)$.

4.1.3 Quadratures on the auxiliary circle

The compression process computes the boundary conditions on Γ_0, and the decompression process solves the EDP (4.1) or IDP (4.4) and evaluates solutions by computing boundary integral by the composite trapezoidal quadrature rule at each discretization point of the rectangular boundary.

Suppose Γ_0 is parameterized by $\mathbf{r}(s) = (x(s), y(s))$, $s \in [0, 2\pi)$ and the parametric interval is partitioned into M equispaced points $s_i = ih$, $h = 2\pi/M$, $i = 0, 1, \cdots, M$. Let $\mathbf{r}'(s) = (x'(s), y'(s))$ be the tangent vector of the curve at the parameter s. Denoting the

integral kernel and the density function as $K(\mathbf{q},\mathbf{p})$ and $\phi(\mathbf{p})$, respectively, then the double layer potential at some point $\mathbf{p}_j$ (the j-th point on Γ_0) could be approximated by the following formulations

$$\int_{\Gamma_0} K(\mathbf{q},\mathbf{p}_j)\phi(\mathbf{q})\,\mathrm{d}s_{\mathbf{q}} \approx 2h \sum_{n=0,2,\cdots}^{M-2} K_{nj}\phi_n|\mathbf{r}'_n|, \quad \text{if } j \text{ is odd;}$$

$$\int_{\Gamma_0} K(\mathbf{q},\mathbf{p}_j)\phi(\mathbf{q})\,\mathrm{d}s_{\mathbf{q}} \approx 2h \sum_{n=1,3,\cdots}^{M-1} K_{nj}\phi_n|\mathbf{r}'_n|, \quad \text{if } j \text{ is even;}$$

where $K_{ij}:=K(\mathbf{r}(t_i),\mathbf{r}(t_j))$, $\phi_j:=\phi(\mathbf{r}(t_j))$ and $\mathbf{r}'_j=\mathbf{r}'(t_j)$. The odd-even alternative technique circumvents the evaluation of singular integrals.

The composite trapezoidal quadrature converges as fast as the spectrum of the integral operator. However, the spectrum of integral operators involving K_0 decay slowly [24]. For the kernel of the double layer integral corresponding to the Laplacian, the Fourier coefficients drop fast, hence the error decays quickly with respect to M. As for that of the modified Helmholtz operator, the Fourier coefficients decays as the rate $\mathcal{O}(n^{-3})$, where n is the Fourier mode, so the trapezoidal quadrature is only a third-order method.

To reach a higher order of convergence, the hybrid Gauss-trapezoidal quadrature rule, which is designed for functions with a logarithmic singularity introduced by Bradley Alpert [8], is employed for the modified Helmholtz case. The hybrid Gauss-trapezoidal quadrature used in this work is of order $\mathcal{O}(h^8\log h)$. The trapezoidal quadrature is used in the interval where is relatively far from the target point t_j while the Gauss quadrature nodes v_n and weights w_n, $n=1,\cdots,l$, are used within the interval $[t_j-ah,t_j+ah]$, where a and l are two positive integers. Using the hybrid Gauss-trapezoidal quadrature rule, the double layer integral is discretized as

$$\begin{aligned}
\int_{\Gamma_0} K(\mathbf{q},\mathbf{p}_j)\phi(\mathbf{q})\,\mathrm{d}s_{\mathbf{q}} \approx{}& h \sum_{n=j+a}^{M+j-a} K_{nj}\phi_n|\mathbf{r}'_n| \\
&+ h \sum_{n=1}^{l} w_n K(\mathbf{r}(t_j+v_nh),\mathbf{r}(t_j))\phi(\mathbf{r}(t_j+v_nh))|\mathbf{r}'(t_j+v_nh)| \\
&+ h \sum_{n=1}^{l} w_n K(\mathbf{r}(t_j-v_nh),\mathbf{r}(t_j))\phi(\mathbf{r}(t_j-v_nh))|\mathbf{r}'(t_j-v_nh)|. \quad (4.7)
\end{aligned}$$

Provided with the density function ϕ at equispaced trapezoidal quadrature points, that at the hybrid Gauss-trapezoidal quadrature points is calculated by Fourier interpolation. This process is accelerated by non-uniform FFT [10, 14].

The quadrature used for the Laplacian kernel is spectrally accurate, while that for the modified Helmholtz kernel is of order $\mathcal{O}(h^8\log h)$. They both can considerably accelerate the computation with a fixed M on Γ_0 since the quadrature is so accurate compared with
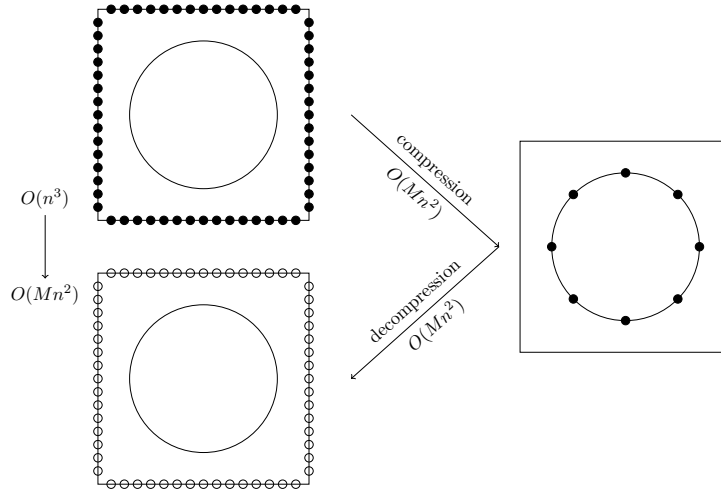
Figure 3: The information of volume integrals on the $\partial\mathcal{B}$ is compressed into that on Γ_0. The compression process is computing volume integrals at M discretization points on the auxiliary circle. The decompression process is solving BIE on Γ_0 and evaluating double layer integrals at each boundary node on $\partial\mathcal{B}$. The compression-decompression technique reduces the computational complexity of the boundary condition evaluation from $\mathcal{O}(n^3)$ to $\mathcal{O}(Mn^2)$ with $M \ll n$.

the second-order FDM-based solver. Suppose the rectangular domain is partitioned into an $n \times n$ Cartesian grid, and the auxiliary circle is discretized with M DoFs, $M \ll n$, then the compression process needs $\mathcal{O}(Mn^2)$ operations. The computational cost of solving the BIE is $\mathcal{O}(M^2)$, and that of evaluating the double layer integrals on the rectangular boundary is $\mathcal{O}(Mn^2)$, so the computational cost of decompression is $\mathcal{O}(Mn^2)$. Without the compression-decompression technique, the total computational complexity of evaluating volume integral on all boundary points is $\mathcal{O}(n^3)$. A schematic diagram for this method is Fig. 3.

When the boundary condition on $\partial\mathcal{B}$ is obtained, the simple interface problem (3.16) is discretized with a corrected finite difference scheme and solved with FFT-based elliptic solvers. The details will be described in a unified frame with the other two simple interface problems associated with double and single layer integrals.

For three-dimensional cases, Γ_0 will be a spherical surface. The computational consumption for evaluating boundary and volume integrals is both expensive. The fast multipole method can reduce the complexity to some extent. Recently, Jun Lai et al. proposed a spectral boundary integral method by using spherical harmonics [17]. We will consider three-dimensional cases in the future.

4.2   Boundary integrals on Cartesian grid nodes

The rectangular domain $\mathcal{B}$ is partitioned into a uniform Cartesian grid along each spatial direction. The simple interface problem is discretized with the corrected finite difference scheme, where corrections are added to the right-hand side keeping the finite difference

matrix unchanged so that FFT-based fast solvers are applicable. Singular integrals on the interface are obtained by two-variable Lagrange polynomial interpolations. There are eight different boundary integral operators in Eqs. (3.10) and (3.11). Note that adjoint double layer integrals or hyper-singular boundary integrals can be represented as linear combinations of the first-order partial derivatives of single or double layer integrals, so $\mathcal{M}\varphi$ and $\mathcal{N}\varphi$ are obtained by solving the interface problem (3.17) at the same time, so as $\mathcal{L}\psi$ and $\mathcal{M}^*\psi$. Moreover, if double and single layer integrals have the same Green function, they can be the unique solution to an interface problem which is the sum of (3.17) and (3.18).

4.2.1　Modifications of the discrete linear system

Consider the unified interface problem below

$$
\begin{aligned}
\mathcal{A}u &= \tilde{f}, && \text{in } \mathcal{B}, \\
[u] &= \varphi, && \text{on } \Gamma, \\
[u_{\mathbf{n}}] &= \psi, && \text{on } \Gamma, \\
u &= \mathcal{M}\varphi - \mathcal{L}\psi + \mathcal{G}f, && \text{on } \partial\mathcal{B}.
\end{aligned}
\tag{4.8}
$$

The rectangular domain $\mathcal{B} = (a,b)\times(c,d)$ is partitioned into a uniform $n\times n$ Cartesian grid with a spacing parameter $h=(b-a)/n=(d-c)/n>0$. For efficient use of FFT-based fast solvers, n is generally a power of 2, i.e., $n=2^k$ for some positive integral k. For $i,j=0,1,\cdots,n-1$, let $x_i=a+ih$ and $y_j=c+ih$ be the coordinates of the horizontal and vertical grid lines, respectively. Denote as $\mathbf{p}_{i,j}=(x_i,y_j)^T$ the (i,j)-th node of the Cartesian grid. The set of all Cartesian grid nodes is denoted by $\mathcal{P}$. The elliptic operator of the simple interface problem (4.8) is discretized with the standard five-point finite difference scheme. The solution $u(\mathbf{p})$ to the simple interface problem (4.8) has a piecewise form

$$
u(\mathbf{p}) = \begin{cases}
u^{(k)}(\mathbf{p}) & \text{if } \mathbf{p}\in\Omega^{(k)}, \quad k=1,2,\cdots,m, \\
u^{(0)}(\mathbf{p}) & \text{if } \mathbf{p}\in\Omega^{(0)}.
\end{cases}
$$

Let $u_{i,j}$ be an approximation of $u(x_i,y_j)$. The five-point finite difference equation reads

$$
\sum_{r,s} a^{(r,s)} u_{i+r,j+s} = \tilde{f}_{i,j}.
\tag{4.9}
$$

Here, the subscripts $r,s=-1,0$ or 1, and $a^{(r,s)}$ is the corresponding non-zero coefficient, they are all of the order $\mathcal{O}(h^{-2})$. It is well-known that the local truncation error of the standard five-point finite difference scheme is $\mathcal{O}(h^2)$ without any interface.

　　The grid nodes are classified as interior, exterior, regular, and irregular nodes, denote

as $\mathcal{P}_i, \mathcal{P}_e, \mathcal{P}_r$ and $\mathcal{P}_s$. They are defined as follows:

$$\mathcal{P}_i := \{\mathbf{p}_{i,j} \in \mathcal{P} \mid \mathbf{p}_{i,j} \in \Omega_i\},$$
$$\mathcal{P}_e := \{\mathbf{p}_{i,j} \in \mathcal{P} \mid \mathbf{p}_{i,j} \notin \Omega_i\},$$
$$\mathcal{P}_r := \{\mathbf{p}_{i,j} \in \mathcal{P} \mid Sten(i,j) \subset \mathcal{P}_i \text{ or } Sten(i,j) \subset \mathcal{P}_e\},$$
$$\mathcal{P}_s := \{\mathbf{p}_{i,j} \in \mathcal{P} \mid \mathbf{p}_{i,j} \notin \mathcal{P}_r\},$$

where $Sten(i,j) := \{(x_i,y_j),(x_{i-1},y_j),(x_{i+1},y_j),(x_i,y_{j-1}),(x_i,y_{j+1})\}$.

Due to the existence of the interface Γ, finite difference discretization usually has large local truncation errors, which may be on the order of $\mathcal{O}(h^{-2})$ at irregular grid nodes. Corrections can be calculated with Taylor expansion [41] or the correction function method [22]. The modified five-point finite difference equation at an irregular grid node reads

$$\sum_{r,s} a^{(r,s)} u_{i+r,j+s} = \tilde{f}_{i,j} + C_{i,j}^{(5)}, \tag{4.10}$$

where $C_{i,j}^{(5)}$ is a first-order approximation to the local truncation error $E_{i,j}$. Let $[u] = u^{(k)} - u^{(0)}$ at (ξ,η), expanding the local truncation error at some nearby point $(\xi,\eta) \in \Gamma$ yields

$$E_{ij} = \sum_{|r|+|s| \neq 0} \alpha_{r,s} \{u^{(k)}(x_{i+r},y_{j+s}) - u^{(0)}(x_{i+r},y_{j+s})\} + \mathcal{O}(h^2)$$

$$= \sum_{|r|+|s| \neq 0} \alpha_{r,s} \left\{ [u] + ([u_x]\tilde{\xi} + [u_y]\tilde{\eta}) + \left(\frac{1}{2}[u_{xx}]\tilde{\xi}^2 + [u_{xy}]\tilde{\xi}\tilde{\eta} + \frac{1}{2}[u_{yy}]\tilde{\eta}^2\right) \right\} + \mathcal{O}(h). \tag{4.11}$$

Here k refers to $\mathbf{p}_{i+r,j+s} \in \Omega^{(k)}$, and $[u]$ represents $u^{(k)} - u^{(0)}$ at (ξ,η). If $\mathbf{p}_{i,j} \in \Omega^{(k)}$, then $\alpha_{r,s} = -a^{(r,s)}$, otherwise $\alpha_{r,s} = a^{(r,s)}$. The summation excludes $\mathbf{p}_{i,j}$ itself since this term is always zero.

The modified five-point finite difference equation at an irregular grid node has a local truncation error on the order of h, which makes the total local truncation error of the discretization difference scheme on the order of h^2 [34]. The modification does not change the coefficient matrix from the standard one, so the corrected linear system can still be efficiently solved with FFT-based fast elliptic solvers.

4.2.2 Calculation for jumps of partial derivatives

The approximation for

$$\{u^{(k)}(x_{i+r_v},y_{j+s_v}) - u^{(0)}(x_{i+r_v},y_{j+s_v})\}$$

needs the jumps $[u],[u_x],[u_y],[u_{xx}],[u_{xy}],[u_{yy}]$. The jump of the function $[u]$ is given by the first jump condition of the simple interface (4.8).
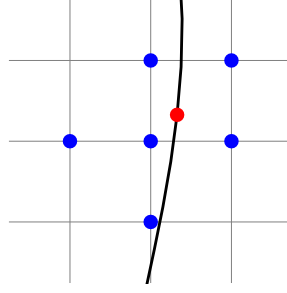
Figure 4: An interpolation stencil for the quadratic interpolation. The six blue dots are source points.

Let $\mathbf{r}(s)$ be the parametric representation of the curve $\Gamma^{(k)}$, where s is the arc length parameter. Computing the tangential derivative of the first jump condition in Eq. (4.8), together with the second jump condition produces a two-by-two linear system

$$\begin{cases} x'(s)[u_x]+y'(s)[u_y]=\varphi_s, \\ y'(s)[u_x]-x'(s)[u_y]=\psi. \end{cases} \tag{4.12}$$

Then computing the tangential derivatives of Eqs. (4.12), respectively, together with the control equation $\mathcal{A}u=\tilde{f}$ (here suppose $\mathcal{A}=\Delta-\kappa^2$) yields a three-by-three linear system

$$\begin{cases} (x')^2[u_{xx}]+2x'y'[u_{xy}]+(y')^2[u_{yy}]=\varphi_{ss}-x''[u_x]-y''[u_y], \\ x'y'[u_{xx}]+\{(y')^2-(x')^2\}[u_{xy}]-x'y'[u_{yy}]=\psi_s-y''[u_x]+x''[u_y], \\ [u_{xx}]+[u_{yy}]=f+\kappa^2[u]. \end{cases} \tag{4.13}$$

The tangential differentiation of the density function is done numerically by the Lagrange interpolation with the discrete data at discretization points of the interface. Solving these linear systems (4.12) and (4.13) gives the jumps of the first and second-order partial derivatives of u on Γ.

4.3 Boundary and volume integrals on the interface

Provided that grid solutions $u_{i,j}$ are obtained by solving the modified finite difference system, the corresponding boundary and volume integrals, and their first-order partial derivatives at discretization points of the interface Γ are evaluated by a two-variable Lagrange polynomial quadratic interpolation.

Assuming the interpolant has the form

$$f(x,y)=c_1+(c_2x+c_3y)+(c_4x^2+c_5xy+c_6y^2).$$

It needs a six-point interpolation stencil (as illustrated in Fig. 4) to determine the coefficients $\{c_\nu\}_{\nu=1}^6$. These interpolation points are denoted by $\{(x_{i+r_\nu},y_{j+s_\nu})\}$, $\nu=1,2,\cdots,6$.

Due to the discontinuity of the solution or/and its partial derivatives across the interface Γ, the polynomial interpolation needs modifications, too. To approximate $u^{(k)}(\mathbf{q}_k)$, the one-sided limit of $u^{(k)}$ at $\mathbf{q}_k \in \Gamma_k$, all stencil points should be modified so that they are equal to their extensions in $\Omega^{(k)}$. If an interpolation point $(x_{i+r_\nu}, y_{j+s_\nu})$ is inside $\Omega^{(l)}$ with $0 < l \neq k$, then the approximation for $u^{(k)}$ at this point is $u_{i+r_\nu, j+s_\nu} + \{u^{(k)}(x_{i+r_\nu}, y_{j+s_\nu}) - u^{(l)}(x_{i+r_\nu}, y_{j+s_\nu})\}$. Here $\{u^{(k)}(x_{i+r_\nu}, y_{j+s_\nu}) - u^{(l)}(x_{i+r_\nu}, y_{j+s_\nu})\}$ is replaced by

$$\{u^{(k)}(x_{i+r_\nu}, y_{j+s_\nu}) - u^{(0)}(x_{i+r_\nu}, y_{j+s_\nu})\} + \{u^{(0)}(x_{i+r_\nu}, y_{j+s_\nu}) - u^{(l)}(x_{i+r_\nu}, y_{j+s_\nu})\}.$$

If an interpolation point $(x_{i+r_\nu}, y_{j+s_\nu})$ is an exterior point, then it is replaced by

$$u_{i+r_\nu, j+s_\nu} + \left(u^{(k)}(x_{i+r_\nu}, y_{j+s_\nu}) - u^{(0)}(x_{i+r_\nu}, y_{j+s_\nu}) \right).$$

The modification for the interpolation scheme is similar to that for the finite difference scheme. The interpolation stencil and coefficient matrix are not changed. Instead, only the discrete data at the grid nodes is adjusted.

5 Algorithm summary

The unbounded interface problem is solved with boundary integral equation methods. Boundary and volume integrals are transformed into equivalent but much simpler bounded interface problems on rectangular domains. The computational complexity of the boundary condition evaluation is reduced by the compression-decompression technique, which is implemented with an auxiliary circle. The rectangular domain is partitioned into a uniform $n \times n$ Cartesian grid. The interface Γ is discretized with N quasi-uniformly nodes, and the auxiliary circle Γ_0 is partitioned into M uniformly nodes.

The algorithm for solving an unbounded interface problem is summarized as follows:

step 1 Compute volume integrals on Γ_0 by direct quadrature, obtain the right-hand side of the BIE (4.2);

step 2 Solving the BIE (4.2) with a fixed low DoFs on the circle.

step 3 Evaluate the double layer integral (4.3) at each discretization point on the rectangular boundary to obtain volume integrals on that.

step 4 Partition the rectangular domain into a uniform Cartesian grid, discretize the simple interface problem (3.16) with corrected finite difference scheme, and solve it with FFT-based fast solvers;

step 5 Compute the box boundary conditions of the simple interface problem (3.17) or (3.18), and solve it like solving (3.16) to obtain the right-hand side of the BIE (3.15) or (3.10) and (3.11);

step 6 Use a Krylov subspace method (e.g., GMRES) to solve the BIE(s). Each iteration needs to compute boundary integrals and extract boundary values and normal derivatives by polynomial interpolation.

step 7 Use density functions to evaluate boundary integrals, and the solution is obtained.

The computational complexity for computing bounded integrals by solving equivalent but much simpler interface problem is $\mathcal{O}(n^2\log n)$. For solving the equivalent simple interface problem corresponding to a volume integral, the computational complexity is also $\mathcal{O}(n^2\log n)$ provided that the boundary conditions evaluation is reduced to $\mathcal{O}(Mn^2)$ by compression-decomposition technique. For Fredholm integral equations of the second kind, the GMRES iteration time is almost constant, since the linear systems arising in the discretization of integral equations are stable [20]. As a result, the total algorithm complexity of solving the unbounded interface problem is $\mathcal{O}(n^2\log n)$.

6   Numerical examples

In this section, we present some numerical examples to test the time complexity and the convergence order of the method. We solve interface problems on refined Cartesian grids with fixed DoFs on the auxiliary circle. At the end of this section, a brief investigation of the effects of the DoFs of the auxiliary circle on the overall accuracy of the algorithm.

We present results for three different problems. The interfaces used in these examples are illustrated in Fig. 5. The rectangular domain is selected to be $\mathcal{B} = (-1.5, 1.5) \times (-1.5, 1.5)$ and the radius of the auxiliary circle is $r = 1.5/\sqrt{2} - 0.2$ in Examples 6.1-6.4. In all these examples, the DoFs on the circle are fixed to be 64, and the DoFs on the interface Γ are equal to the size of the Cartesian grid. The order p used to quadrature is set to be 8. The tolerance used in the GMRES iteration is 10^{-10}.

This algorithm is implemented in codes written in the `C++` computer language. The Bessel function is evaluated with `C++` build-in functions. All these numerical examples are performed in double precision on a desktop computer with Intel(R) Core(TM) i7-10700K 3.80GHz CPU.

Example 6.1. This example displays a special case, where difference operators are both Laplacian, i.e., $\mathcal{A}_i = \mathcal{A}_e = \Delta$. The bounded domain Ω_i is a rotated ellipse with major and minor radii 0.8 and 0.6, see the left one in Fig. 5. We choose conductivity parameters $\sigma_i = 1$ and $\sigma_e = 3$. The interface data $g(\mathbf{p}), j(\mathbf{p})$ and the source term $f(\mathbf{p})$ are selected so that the exact solution to the interface problem is

$$u_i(\mathbf{p}) = x + e^{0.6x+0.8y}, \quad \text{in } \Omega_i,$$

$$u_e(\mathbf{p}) = \frac{-x}{x^2+y^2}, \quad \text{in } \Omega_e.$$

Fig. 6(a) illustrates the rectangular domain $\mathcal{B}$, the interface Γ, and the isoline of the potential function $u(\mathbf{p})$. The max-error in a 512×512 Cartesian grid is illustrated in Fig. 6(c).

(a) rotated ellipse curve   (b) star-shaped curve   (c) ellipses
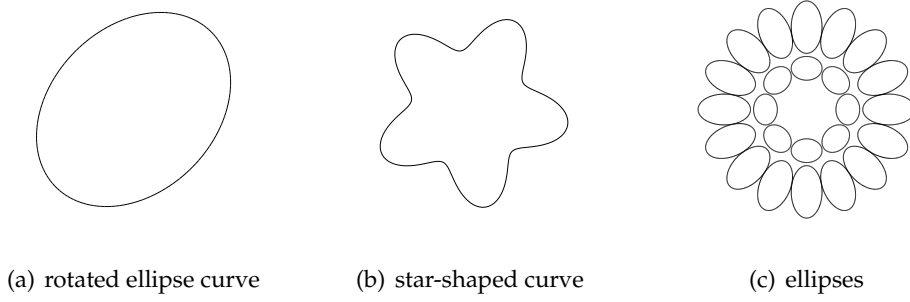
Figure 5: Interfaces used in numerical examples.

Table 1: Numerical results of Example 6.1: #GMRES is the iteration number of GMRES for solving the BIE of the interface problem. $\|\mathbf{e}_h^{int}\|_\infty$ is the max-error of numerical solution inside, $\|\mathbf{e}_h^{ext}\|_\infty$ is the max-error of numerical solution outside, $\|\mathbf{e}_h^{int}\|_2$ is the root-mean-square error of numerical solution inside, $\|\mathbf{e}_h^{ext}\|_2$ is the root-mean-square error of numerical solution outside.

grid size	256×256	512×512	1024×1024	2048×2048
] #GMRES	6	5	5	5
$\|\mathbf{e}_h^{int}\|_\infty$	3.10e-05	4.94e-06	1.64e-06	3.06e-07
$\|\mathbf{e}_h^{ext}\|_\infty$	4.70e-05	1.07e-05	2.99e-06	6.32e-07
$\|\mathbf{e}_h^{int}\|_2$	8.06e-06	1.83e-06	4.80e-07	1.14e-07
$\|\mathbf{e}_h^{ext}\|_2$	1.32e-05	3.27e-06	8.13e-07	2.02e-07
CPU(secs)	1.82e-01	6.56e-01	2.63e+00	1.14e+01

Table 1 shows the max-error and root-mean-square error inside and outside, respectively, which verifies the second-order convergence. It also displays the iteration number of GMRES solving the BIE of the unbounded interface problem, which is nearly a constant. The total computational time is listed in the last row of Table 1, which confirms the $\mathcal{O}(n^2)$ computational complexity.

Example 6.2. This example repeats the same test as Example 6.1, but with the interface depicted in the middle of Fig. 5 and with the conductivity parameters $\sigma_i = 1$ and $\sigma_e = 3 \times 10^4$.

Fig. 6(b) illustrates the rectangular domain $\mathcal{B}$, the interface Γ, and the isoline of the potential function $u(\mathbf{p})$. Fig. 6(d) illustrates the max-error in a 512×512 Cartesian grid. The max-error and root-mean-square error inside and outside, the iteration number of GMRES of solving the BIE of the unbounded interface problem, and the total computational time are displayed in Table 2. The second-order convergence and $\mathcal{O}(n^2 \log n)$ computational complexity are verified.
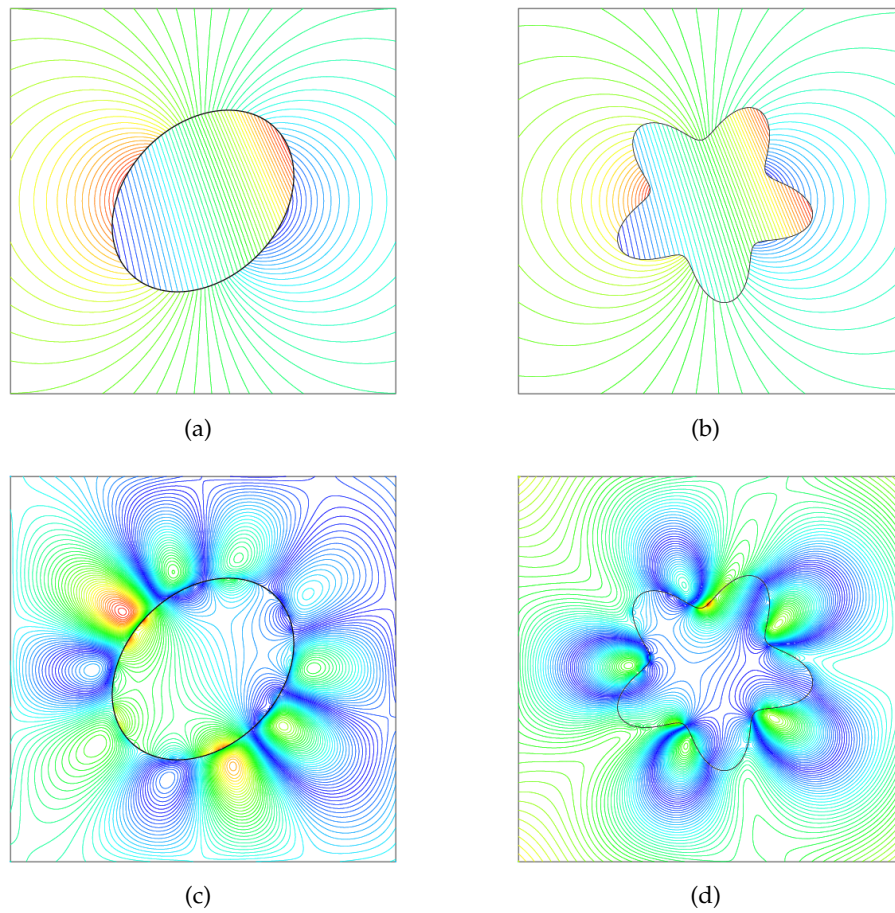
(a)

(b)

(c)

(d)

Figure 6: (a) The isoline plot of the potential in Example 6.1; (b) the isoline plot of the potential in Example 6.2; (c) the max-error plot in a 512×512 grid in Example 6.1; (d) the max-error plot in a 512×512 grid in Example 6.2.

Table 2: Numerical results of Example 6.2.

grid size	256×256	512×512	1024×1024	2048×2048
#GMRES	14	13	12	12
$\|\mathbf{e}_h^{int}\|_\infty$	1.48e-04	1.79e-05	4.16e-06	1.09e-06
$\|\mathbf{e}_h^{ext}\|_\infty$	1.54e-04	1.75e-05	4.49e-06	1.24e-06
$\|\mathbf{e}_h^{int}\|_2$	3.80e-05	3.54e-06	1.02e-06	3.39e-07
$\|\mathbf{e}_h^{ext}\|_2$	2.73e-05	6.90e-06	1.92e-06	4.88e-07
CPU(secs)	4.37e-01	1.64e+00	6.26e+00	2.60e+01

Table 3: Numerical results of Example 6.3.

grid size	256×256	512×512	1024×1024	2048×2048
#GMRES	16	15	14	14
$\|\mathbf{e}_h^{int}\|_\infty$	2.43e-05	3.57e-06	7.54e-07	1.48e-07
$\|\mathbf{e}_h^{ext}\|_\infty$	2.53e-05	3.69e-06	7.62e-07	1.48e-07
$\|\mathbf{e}_h^{int}\|_2$	5.06e-06	1.01e-06	2.43e-07	6.33e-08
$\|\mathbf{e}_h^{ext}\|_2$	4.04e-06	7.69e-07	1.67e-07	3.93e-08
CPU(secs)	1.85e+00	6.93e+00	2.64e+01	1.05e+02

Table 4: Numerical results of Example 6.4.

grid size	256×256	512×512	1024×1024	2048×2048
#GMRES	57	61	59	66
$\|\mathbf{e}_h^{int}\|_\infty$	9.92e-05	1.12e-05	2.83e-06	2.99e-07
$\|\mathbf{e}_h^{ext}\|_\infty$	7.24e-05	5.95e-06	2.71e-07	4.34e-08
$\|\mathbf{e}_h^{int}\|_2$	4.91e-05	2.03e-06	2.30e-06	2.13e-07
$\|\mathbf{e}_h^{ext}\|_2$	1.18e-05	8.55e-07	9.60e-08	1.19e-08
CPU(secs)	1.98e+01	8.37e+01	3.22e+02	1.44e+03

Example 6.3. In this example, the elliptic operators are both modified Helmholtz $\mathcal{A}_i = \mathcal{A}_e = \Delta - \kappa^2$ with $\kappa^2 = 2$. The interface Γ is a star-shaped curve, illustrated in the middle of Fig. 5.

The conductivity parameters are chosen to be $\sigma_i = 1$ and $\sigma_e = 3\times10^4$. The interface data $g(\mathbf{p}), j(\mathbf{p})$ and the source term $f(\mathbf{p})$ are selected so that the exact solution to the interface problem is

$$u_i(\mathbf{p}) = \sinh(x+y), \quad \text{in } \Omega_i,$$

$$u_e(\mathbf{p}) = \frac{1}{2\pi}K_0(\kappa\mathbf{p}), \quad \text{in } \Omega_e.$$

The solution and the max-error in a 512×512 grid are illustrated in Fig. 7(a) and 7(c), respectively. Table 3 shows the computational results of Example 6.3.

Example 6.4. This example repeats the test in Example 6.3, but with an alternatively star-shaped interface and with different wave numbers $\kappa_i^2 = 3$ and $\kappa_e^2 = 1$. The conductivities are $\sigma_i = 1$ and $\sigma_e = 3\times10^4$. The computational results are displayed in Fig. 7(b)(d) and Table 4.

Example 6.5. This example is a general case, the elliptic operators inside and outside are modified Helmholtz with different wave numbers, i.e., $\mathcal{A}_i = \Delta - \kappa_i^2$ and $\mathcal{A}_e = \Delta - \kappa_e^2$ with $\kappa_i = 1$ and $\kappa_e = 4$. The inside domain $\Omega_i = \cup_{k=1}^{24}\Gamma_k$ is multi-connected, which is consists

(a)   (b)

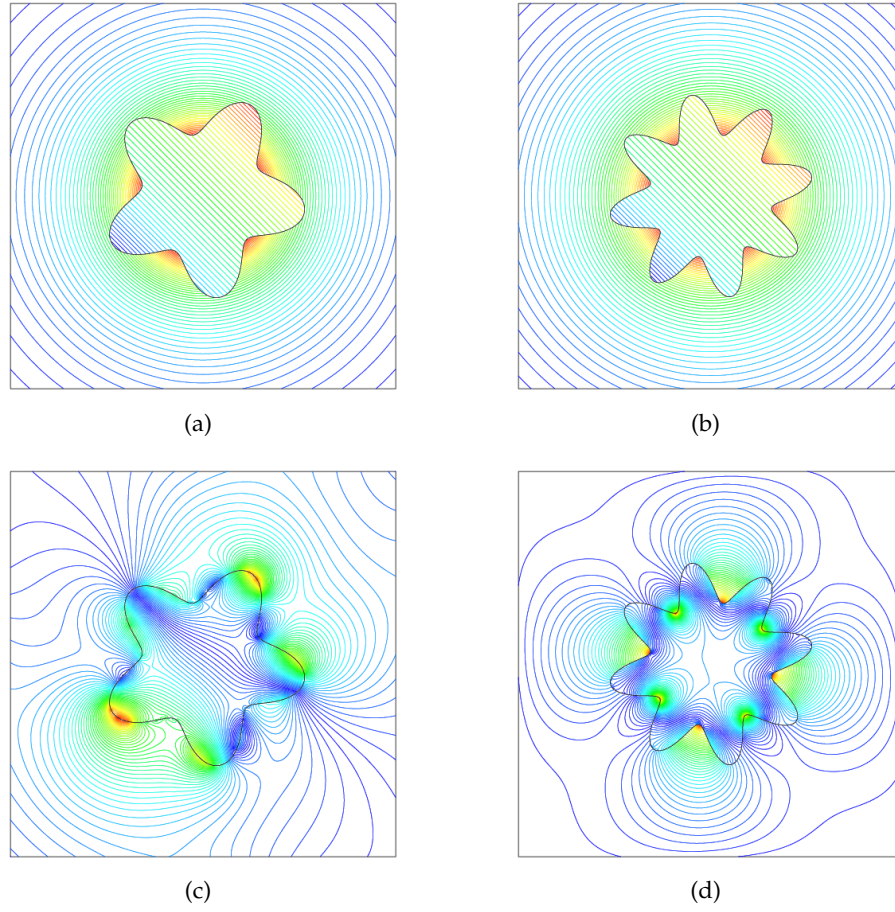(c)   (d)

Figure 7: (a) The isoline plot of the potential in Example 6.3; (b) the isoline plot of the potential in Example 6.4; (c) the max-error plot in a 512×512 grid in Example 6.3; (d) the max-error plot in a 512×512 grid in Example 6.4.

of 24 ellipses, see Fig. 5 (right) for illustration. Two adjacent ellipses among them are almost in touch with a distance of about 10^{-3}. The conductivity parameters are $\sigma_i = 1$ and $\sigma_e = 2$. The interface data $g(\mathbf{p}), j(\mathbf{p})$ and the source term $f(\mathbf{p})$ are selected so that the exact solution to the interface problem is

$$u_i(\mathbf{p}) = \sinh(x+y), \quad \text{in } \Omega_i,$$

$$u_e(\mathbf{p}) = \sum_{k=1}^{24} K_0(\kappa_e |\mathbf{q}_k - \mathbf{p}|), \quad \text{in } \Omega_e.$$

Here these points, $\mathbf{q}_k$, $k = 1, 2 \cdots, 24$, are centers of circles.

The rectangular domain $\mathcal{B}$ is selected to be $\mathcal{B} = (-1.0, 1.0) \times (-1.0, 1.0)$. The bigger rectangular domain $\tilde{\mathcal{B}}$ is twice the size of $\mathcal{B}$. The auxiliary circle with radius $r = \sqrt{2} + 0.5$
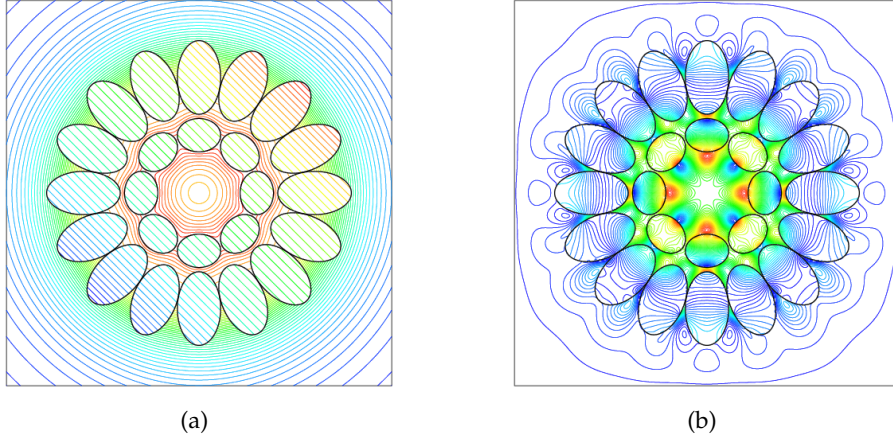
(a)   (b)

Figure 8: (a) The isoline plot of the potential for Example 6.5; (b) the max-error plot in a 512×512 grid for Example 6.5.

Table 5: Numerical results of Example 6.5.

grid size	256×256	512×512	1024×1024	2048×2048
#GMRES	23	23	26	25
$\|\mathbf{e}_h^{int}\|_\infty$	1.94e-03	2.67e-04	6.08e-05	6.99e-06
$\|\mathbf{e}_h^{ext}\|_\infty$	1.31e-03	1.90e-04	6.89e-05	1.38e-05
$\|\mathbf{e}_h^{int}\|_2$	6.45e-04	7.56e-05	1.71e-05	2.56e-06
$\|\mathbf{e}_h^{ext}\|_2$	3.09e-04	4.13e-05	1.60e-05	2.94e-06
CPU(secs)	1.38e+02	5.50e+02	2.44e+03	9.44e+03

and fixed DoFs $M=32$ locates between the two rectangles. The DoFs of each Γ_k are equal to the size of the Cartesian grid. The tolerance used in the GMRES iteration is 10^{-8}.

The solution to this unbounded interface problem is illustrated in Fig. 8. The computational results are displayed in Table 5.

Example 6.6. In this example, we test the influence of the DoFs of the auxiliary circle on the computational errors. We fixed the Cartesian grid to be $I=J=256$ and test different M's.

Fig. 9(a) illustrates the change of interior errors along with M, and Fig. 9(b) illustrates the change of exterior errors along with M. These numbers $1-4$ refer to Examples 6.1-6.4, respectively. From these plots, one observed that the errors do not get lower along with the increase of M. This is reasonable, as the spectral convergence of the composite trapezoidal rule for periodic smooth function. So, choosing M relatively small is enough to guarantee numerical accuracy.
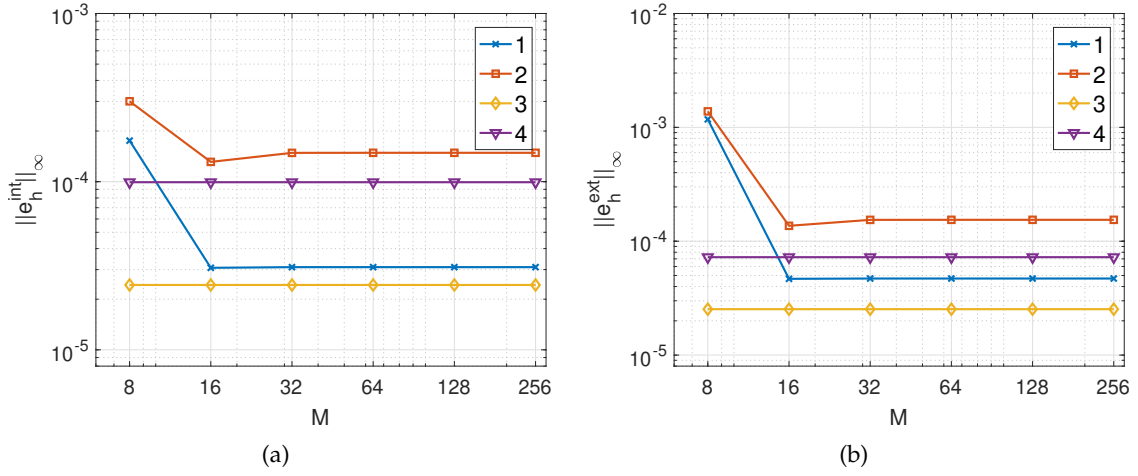
Figure 9: Fix the Cartesian grid to be 256×256, change M from 8 to 256. (a) the errors of u_i in solving the unbounded interface problem, it decays to 10^{-4} before $M = 32$. (b) the errors of u_e in solving the unbounded interface problem, it decays to 10^{-3} before $M = 32$.

7 Discussion

In this work, the unbounded interface problem with a non-homogeneous source term is solved with boundary integral equation methods. The boundary or the volume integral is transformed into an equivalent but much simpler bounded interface problem on a rectangular domain, which is discretized with a corrected finite difference scheme and is solved with FFT-based elliptic fast solvers. The far-field condition is converted to the boundary and volume integrals on the rectangular boundary $\partial \mathcal{B}$. The boundary condition of the boundary integral on the rectangular boundary is non-singular, which is evaluated by the composite trapezoidal quadrature. But the direct evaluation of the volume integral on the rectangular boundary has relatively high computational complexity. An auxiliary circle is introduced to reduce the complexity. The information of volume integrals at discretization points on the rectangular boundary is compressed into that at a fixed number of discretization points on the auxiliary circle. It is restored by decompressing by solving a boundary integral equation on the circle and evaluating double layer integrals on the rectangular boundary. Since the high accuracy for solving the boundary integral equation, the discretization points on the circle are fixed, and the number of discretization points is small. This reduces the total algorithm complexity from $\mathcal{O}(n^3)$ to $\mathcal{O}(n^2 \log n)$.

The method presented in this work can be used to solve the multi-phase Stokes flow, acoustic scattering problem in an unbounded domain. Besides, the fast volume integral evaluation technique can be extended for the elliptic interface problem on an unbounded domain in three space dimensions.

Acknowledgments

References

[1] Daniel Baffet, Thomas Hagstrom, and Dan Givoli. Double absorbing boundary formulations for acoustics and elastodynamics. *SIAM Journal on Scientific Computing*, 36(3):A1277–A1312, 2014.

[2] Alvin Bayliss and Eli Turkel. Radiation boundary conditions for wave-like equations. *Communications on Pure and Applied Mathematics*, 33(6):707–725, 1980.

[3] J. Thomas Beale, Wenjun Ying, and Jason R. Wilson. A simple method for computing singular or nearly singular integrals on closed surfaces. *Communications in Computational Physics*, 20(3):733–753, 2016.

[4] Jean-Pierre Berenger. A perfectly matched layer for the absorption of electromagnetic waves. *Journal of Computational Physics*, 114(2):185–200, 1994.

[5] Jean-Pierre Berenger. Three-dimensional perfectly matched layer for the absorption of electromagnetic waves. *Journal of Computational Physics*, 127(2):363–379, 1996.

[6] George Biros, Lexing Ying, and Denis Zorin. A fast solver for the Stokes equations with distributed forces in complex geometries. *Journal of Computational Physics*, 193(1):317–348, 2004.

[7] John P. Boyd. Spectral methods using rational basis functions on an infinite interval. *Journal of Computational Physics*, 69(1):112–142, 1987.

[8] Bradley K. Alpert. Hybrid Gauss-trapezoidal quadrature rules. *SIAM Journal on Scientific Computing*, 20(5):1551–1584, January 1999.

[9] G. F. Carrier. Singular perturbation theory and geophysics. *SIAM Review*, 12(2):175–193, April 1970.

[10] A. Dutt and V. Rokhlin. Fast Fourier transforms for nonequispaced data. *SIAM Journal on Scientific Computing*, 14(6):1368–1393, November 1993.

[11] Roland W. Freund, Gene H. Golub, and Noël M. Nachtigal. Iterative solution of linear systems. *Acta Numerica*, 1:57–100, January 1992.

[12] Gang Bao and Weiwei Sun. A fast algorithm for the electromagnetic scattering from a large cavity. *SIAM Journal on Scientific Computing*, 27(2):553–574, January 2005.

[13] G.N Watson. *A Treatise on the Theory of Bessel Functions*. Cambridge Univ. Press, London/New York, 2nd ed. edition, 1944.

[14] Leslie Greengard and June-Yub Lee. Accelerating the nonuniform fast Fourier transform. *SIAM Review*, 46(3):443–454, January 2004.

[15] Ben-Yu Guo, Jie Shen, and Zhong-Qing Wang. A rational approximation and its applications to differential equations on the half line. *Journal of Scientific Computing*, 15(2):117–147, 2000.

[16] Thomas Hagstrom. Radiation boundary conditions for the numerical simulation of waves. *Acta Numerica*, 8:47–106, January 1999.

[17] Heping Dong, Jun Lai, and Peijun Li. A spectral boundary integral method for the elastic obstacle scattering problem in three dimensions. *Journal of Computational Physics*, 469:111546, November 2022.

[18] George C. Hsiao and Wolfgang L. Wendland. *Boundary Integral Equations*, volume 164 of *Applied Mathematical Sciences*. Springer Berlin Heidelberg, Berlin, Heidelberg, 2008.

[19] Sharad Kapur and Vladimir Rokhlin. High-Order Corrected Trapezoidal Quadrature Rules for Singular Functions. *SIAM Journal on Numerical Analysis*, 34(4):1331–1356, August 1997.

[20] Rainer Kress. *Linear Integral Equations*, volume 82 of *Applied Mathematical Sciences*. Springer New York, New York, NY, 2014.

[21] Arvid T. Lonseth. Sources and applications of integral equations. *SIAM Review*, 19(2):241–278, April 1977.

[22] Alexandre Noll Marques, Jean-Christophe Nave, and Rodolfo Ruben Rosales. A correction function method for poisson problems with interface jump conditions. *Journal of Computational Physics*, 230(20):7567–7597, 2011.

[23] Mary Catherine A. Kropinski and Bryan D. Quaife. Fast integral equation methods for the modified Helmholtz equation. *Journal of Computational Physics*, 230(2):425–434, January 2011.

[24] Mary Catherine A. Kropinski and Bryan D. Quaife. *Fast integral equation methods for the modified Helmholtz equation*. A Thesis submitted in partial fulfillment of the requirements for the degree of Doctor of Philosophy, Simon Fraser University, January 2011.

[25] Arnold Neumaier. Molecular modeling of proteins and mathematical prediction of protein structure. *SIAM Review*, 39(3):407–460, January 1997.

[26] David P. Nicholls and Nilima Nigam. Exact non-reflecting boundary conditions on general domains. *Journal of Computational Physics*, 194(1):278–303, 2004.

[27] David P. Nicholls and Fernando Reitich. Stability of high-order perturbative methods for the computation of Dirichlet–Neumann operators. *Journal of Computational Physics*, 170(1):276–298, 2001.

[28] David P. Nicholls and Jie Shen. A stable high-order method for two-dimensional bounded-obstacle scattering. *SIAM Journal on Scientific Computing*, 28(4):1398–1419, January 2006.

[29] Rikard Ojala and Anna-Karin Tornberg. An accurate integral equation method for simulating multi-phase Stokes flow. *Journal of Computational Physics*, 298:145–160, 2015.

[30] Jie Shen. Stable and efficient spectral methods in unbounded domains using Laguerre functions. *SIAM Journal on Numerical Analysis*, 38(4):1113–1133, January 2000.

[31] Jie Shen and Li-Lian Wang. Some recent advances on spectral methods for unbounded domains. *Communications in Computational Physics*, 5, February 2009.

[32] Jie Shen and Haijun Yu. Efficient spectral sparse grid methods and applications to high-dimensional elliptic equations II. Unbounded domains. *SIAM Journal on Scientific Computing*, 34(2):A1141–A1164, January 2012.

[33] Tao Yin, George C. Hsiao, and Liwei Xu. Boundary integral equation methods for the two-dimensional fluid-solid interaction problem. *SIAM Journal on Numerical Analysis*, 55(5):2361–2393, January 2017.

[34] Thomas Beale and Anita Layton. On the accuracy of finite difference methods for elliptic problems with interfaces. *Communications in Applied Mathematics and Computational Science*, 1(1):91–119, December 2006.

[35] H. A. van der Vorst. Bi-CGSTAB: A fast and smoothly converging variant of Bi-CG for the solution of non-symmetric linear systems. *SIAM Journal on Scientific and Statistical Computing*, 13(2):631–644, March 1992.

[36] Shravan K. Veerapaneni, Denis Gueyffier, Denis Zorin, and George Biros. A boundary in-

tegral method for simulating the dynamics of inextensible vesicles suspended in a viscous fluid in 2D. *Journal of Computational Physics*, 228(7):2334–2353, 2009.

[37] Mingtao Xia, Sihong Shao, and Tom Chou. Efficient scaling and moving techniques for spectral methods in unbounded domains. *SIAM Journal on Scientific Computing*, 43(5):A3244–A3268, January 2021.

[38] Xin-min Xiang and Zhong-qing Wang. Generalized Hermite spectral method and its applications to problems in unbounded domains. *SIAM Journal on Numerical Analysis*, 48(4):1231–1253, January 2010.

[39] Yaning Xie and Wenjun Ying. A fourth-order kernel-free boundary integral method for implicitly defined surfaces in three space dimensions. *Journal of Computational Physics*, 415:109526, August 2020.

[40] Zhiguo Yang, Li-Lian Wang, and Yang Gao. A truly exact perfect absorbing layer for time-harmonic acoustic wave scattering problems. *SIAM Journal on Scientific Computing*, 43(2):A1027–A1061, 2021.

[41] Wenjun Ying. A Cartesian grid-based boundary integral method for an elliptic interface problem on closely packed cells. *Communications in Computational Physics*, 24(4):1196–1220, 2018.

[42] Wenjun Ying and Craig S. Henriquez. A kernel-free boundary integral method for elliptic boundary value problems. *Journal of Computational Physics*, 227(2):1046–1074, 2007.

[43] Wenjun Ying and Wei-Cheng Wang. A kernel-free boundary integral method for implicitly defined surfaces. *Journal of Computational Physics*, 252:606–624, 2013.

[44] Wenjun Ying and Wei-Cheng Wang. A kernel-free boundary integral method for variable coefficients elliptic PDEs. *Communications in Computational Physics*, 15(4):1108–1140, April 2014.

[45] Youcef Saad and Martin H. Schultz. GMRES: A generalized minimal residual algorithm for solving non-symmetric linear systems. *SIAM Journal on Scientific and Statistical Computing*, 7(3):856–869, July 1986.

[46] Alexander Z. Zinchenko, Michael A. Rother, and Robert H. Davis. A novel boundary-integral algorithm for viscous interaction of deformable drops. *Physics of Fluids*, 9(6):1493–1511, June 1997.